

UNCLASSIFIED

**Defense Technical Information Center
Compilation Part Notice**

ADP014228

TITLE: Development of Parallel Dip Pen Nanolithography Probe Arrays
for High Throughput Nanolithography

DISTRIBUTION: Approved for public release, distribution unlimited

This paper is part of the following report:

TITLE: Materials Research Society Symposium Proceedings, Volume 758
Held in Boston, Massachusetts on December 3-5, 2002. Rapid Prototyping
Technologies

To order the complete compilation report, use: ADA417756

The component part is provided here to allow users access to individually authored sections of proceedings, annals, symposia, etc. However, the component should be considered within the context of the overall compilation report and not as a stand-alone technical report.

The following component part numbers comprise the compilation report:
ADP014213 thru ADP014236

UNCLASSIFIED

Development of Parallel Dip Pen Nanolithography Probe Arrays for High Throughput Nanolithography

David A. Bullen¹, Xuefeng Wang¹, Jun Zou¹, Sung-Wook Chung², Chang Liu¹, and Chad A. Mirkin²

¹Micro and Nanotechnology Laboratory, University of Illinois at Urbana-Champaign, Urbana, IL, 61801

²Department of Chemistry, Northwestern University, Chicago, IL

ABSTRACT

Dip Pen Nanolithography (DPN) is a lithographic technique that allows direct deposition of chemicals, metals, biological macromolecules, and other molecular "inks" with nanometer dimensions and precision. This paper addresses recent developments in the design and demonstration of high-density multiprobe DPN arrays. High-density arrays increase the process throughput over individual atomic force microscope (AFM) probes and are easier to use than arrays of undiced commercial probes. We have demonstrated passive arrays made of silicon (8 probes, 310 μm tip-to-tip spacing) and silicon nitride (32 probes, 100 μm tip-to-tip spacing). We have also demonstrated silicon nitride "active" arrays (10 probes, 100 μm tip-to-tip spacing) that have embedded thermal actuators for individual probe control. An optimization model for these devices, based on a generalized multilayer thermal actuator, is also described.

INTRODUCTION

Dip Pen Nanolithography (DPN) is a recently introduced [1] method of scanning probe lithography that offers significant advantages over other lithographic processes. In this method, chemicals are adsorbed onto an AFM probe then deposited on a surface by diffusion from the tip while scanning in contact mode. The most common probe is a silicon nitride AFM tip that has been coated by dipping it in a chemical solution or by evaporation from a heated source.

DPN has been successfully applied to a wide variety of patterning tasks. It has been used to pattern biological macromolecules such as thiol-modified ssDNA [2], collagen (via direct patterning) [3], and rabbit immunoglobulin G (via selective adsorption onto 16-mercaptohexadecanoic acid patterns) [4]. The meniscus that forms between the probe tip and substrate in air has been used as a nanoscale chemical reactor to pattern sol-gel precursors [5], a variety of metals [6,7], and conducting polymers [8]. Surface binding in these demonstrations ranges from strong covalent bonds, as in the thiol-gold [1] and silane-oxide [9] systems, to weaker electrostatic, van der Waals, hydrophobic, and hydrogen bonds [10]. In some cases, the covalent chemistries have been shown strong enough to act as masks in various substrate etching applications [11,14].

The wide variety of tasks for which DPN has been used is an indicator of its potential for commercialization, but success will require more than just robust chemistry systems. The real power of DPN can only be unlocked with pattern generation capabilities that far exceed those of single probe systems. The first attempt at multiprobe patterning [12] used a 1-D array of undiced commercial probes. Although this method works, the arrays are so wide (~1.5mm per probe) that array-to-surface misalignment limits the array size with little gain in pattern density. We have

developed a variety of high-density, one-dimensional, passive and active probe arrays that satisfy the need for true high-density pattern generation.

PASSIVE PROBE ARRAYS

We have demonstrated passive high-density probe arrays [13] with tip-to-tip spacing that is more than an order of magnitude better than what is achievable using commercial probes. The arrays are easier to align with the substrate and function in a wide variety of AFMs. SEM micrographs of the devices are shown in Figure 1. One design consists of silicon nitride probes that are $375\text{ }\mu\text{m}$ long (base to probe tip), $50\text{ }\mu\text{m}$ wide, 600nm thick, and have a tip-to-tip spacing of $100\text{ }\mu\text{m}$. The probes have an analytically estimated spring constant of 0.018 N/m and have been used for lithography and topographic imaging [13]. Another design uses silicon probes with beams that are $15\text{ }\mu\text{m}$ wide and $5\text{ }\mu\text{m}$ thick. The tip-to-tip spacing is $310\text{ }\mu\text{m}$. The suspension is folded to increase the beam's effective length and lower its spring constant to an FEA estimated value of 0.315 N/m . They have been used in lithography and tapping mode imaging applications [13]. Figure 2 shows examples of imaging and lithographic results from both designs. All lithography was performed using 1-octadecanethiol (ODT) on a gold substrate.

The fabrication of these devices has been previously described [14] and is summarized here. The probe tips are first formed by anisotropically etching the surface of a $\langle 100 \rangle$ silicon wafer, followed by oxidation sharpening [15]. For silicon nitride probes, the wafer is coated with low

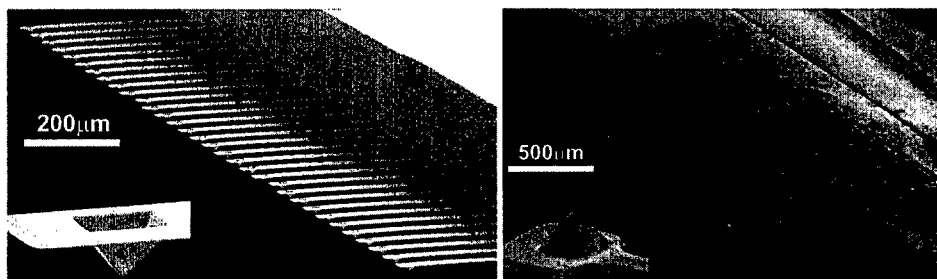


Figure 1. (Left) A passive array of 32 rectangular silicon nitride DPN probes. (Right) A passive array of eight folded-beam silicon DPN probes.

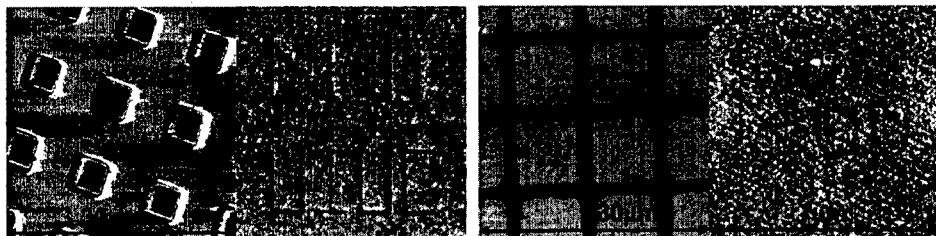


Figure 2. (Left two images) A contact mode calibration grating image and ODT pattern from a passive silicon nitride DPN probe. The ODT characters are $5\text{ }\mu\text{m}$ tall and the line width is 260nm . (Right two images) A tapping mode calibration grating image and ODT pattern from a passive silicon DPN probe. The ODT characters are $1.5\text{ }\mu\text{m}$ tall and the line width is 60nm .

pressure chemical vapor deposited (LPCVD) silicon nitride and the beams are etched out using reactive ion etching. The beams are then released by anisotropic wet etching from the front side of the wafer. For silicon devices, the beams are etched out of an implanted boron etch stop layer and the remaining silicon is removed by anisotropic wet etching.

ACTIVE PROBE ARRAYS

Active probe arrays contain actuators within each probe to lift individual tips off the surface. This allows different patterns to be written by different probes when all probes travel the same path. For our case, thermal actuation was chosen for its large deflection, fabrication simplicity, and robust operation. The active probe arrays consist of a linear array of cantilever beams, each having its own joule heater, silicon nitride/gold bimetallic thermal actuator, and tip. An SEM micrograph of an array is shown in Figure 3 along with an illustration of its operating principle. When the heater is energized, the probes are hot and the tips are lifted from the surface to suspend lithography. When the heater is de-energized, the probe is cool, the tips are pressed against the surface, and lithography is performed in contact mode. The fabrication process for these devices is an extension of the process used to make the devices in Figure 1. The only difference is the addition of steps to evaporate and pattern a chrome/gold layer before the final release etch. This layer forms the heater, power leads, and actuator.

N-layer thermal actuator modeling

Although these devices are referred to as bimetallic thermal actuators, they are actually three layer devices due to the need for an adhesion layer. Many deflection models have been published on the bimetallic case [16-22] but we have found that approximating multilayer (>2 layers) devices as bilayer devices can lead to significant error when estimating tip deflection. Most practical devices need additional layers for promoting adhesion or electrical isolation. As a result of this deficiency, we have created a more general model that characterizes cantilevers with an arbitrary number of layers, each having its own width, thickness, modulus of elasticity, thermal expansion coefficient, and intrinsic stress state. The beam radius of curvature is calculated by summation across some or all of the layers of the structure and may be applied to uses beyond

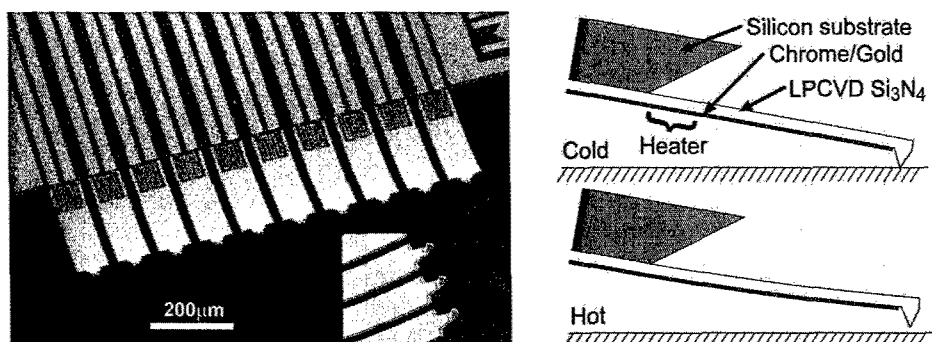


Figure 3. (Left) An array of ten 295 μm long, thermally actuated DPN probes. **(Right)** Thermally actuated DPN probe operation. Heated probes deflect away from the surface.

this particular situation. An abbreviated derivation follows.

Given a beam with n material layers, numbered $i=1$ to n , the first task is to find the location of the neutral axis using the effective width technique [23]. After canceling the elastic modulus of the reference material, the distance between the neutral axis and the bottom of the beam is given by

$$\bar{y} = \frac{\sum_{i=1}^n E_i w_i t_i \left(\frac{t_i}{2} + \sum_{j=1}^{i-1} t_j \right)}{\sum_{i=1}^n E_i w_i t_i}, \quad (1)$$

where E is the modulus of elasticity, w is the width, and t is the thickness of the i th layer. The outer summation (i) is applied over all layers while the inner summation (j) is over the layers below layer i . The term in parenthesis is the distance from the bottom of the beam to the middle of the i th layer. The flexural stiffness of the beam is found using the effective width technique and the parallel axis theorem and is given by

$$I_{\text{eff}} E_o = \sum_{i=1}^n \left[\frac{E_i w_i t_i^3}{12} + E_i w_i t_i \left(\left(\frac{t_i}{2} + \sum_{j=1}^{i-1} t_j \right) - \bar{y} \right)^2 \right], \quad (2)$$

where E_o is an arbitrary reference modulus.

The radius of curvature of the operating actuator results from four sequential processes: (1) layer deposition with a preexisting stress, (2) patterning of all layers to a uniform length, (3) relaxation following release from the substrate, and (4) heating or cooling to the operating temperature. The stress state in each layer is the sum of a uniform component and an assumed linear gradient and is, in general, unrelated to the stress in the other layers. The total strain in a given layer i can be found by superimposing the strain due to uniform intrinsic stress, thermal expansion, and the change in beam length

$$\epsilon_i = \frac{\sigma_{i,\text{unif}} (1 - \nu_i)}{E_i} - \alpha_i \Delta T + \ln \left(\frac{L_{\text{beam}}}{L_{\text{patterned}}} \right), \quad (3)$$

where ν is the poisson's ratio, $\sigma_{i,\text{unif}}$ is the biaxial hydrostatic stress, α is the thermal expansion coefficient, ΔT is the change in temperature of the entire beam, $L_{\text{patterned}}$ is the patterned length of the beam before release from the substrate, and L_{beam} is the final length of the beam after release and heating. Since the cantilever beam carries no axial load, the force exerted by each layer due to internal stresses is given by $P = E w t \epsilon$ and must sum to zero giving

$$\sum_{i=1}^n P_i = \ln \left(\frac{L_{\text{beam}}}{L_{\text{patterned}}} \right) \sum_{i=1}^n E_i w_i t_i + \sum_{i=1}^n (w_i t_i \sigma_{i,\text{unif}} (1 - \nu_i) - E_i w_i t_i \alpha_i \Delta T) = 0. \quad (4)$$

Equation (4) can be solved for the strain due to the change in beam length, given by $\ln(L_{\text{beam}}/L_{\text{patterned}})$. Substituting this result into (3) yields the total strain in layer i . The total strain is then used to find the force and moment exerted by each layer on the beam. Summing these moments gives the total moment within the beam due to thermal stress and uniform intrinsic stresses,

$$M_{\text{uni}} = \sum_{i=1}^n \left[E_i w_i t_i \left(\frac{\sigma_{i,\text{unif}} (1 - \nu_i)}{E_i} - \alpha_i \Delta T - \frac{\sum_{i=1}^n w_i t_i (\sigma_{i,\text{unif}} (1 - \nu_i) - E_i \alpha_i \Delta T)}{\sum_{i=1}^n E_i w_i t_i} \right) \left(\frac{t_i}{2} + \sum_{j=1}^{i-1} t_j \right) \right] \quad (5)$$

A stress gradient may also be present in each layer resulting from changes in the film growth conditions during deposition. Assuming that this stress gradient is linear and uniform in the plane of the film, the total moment exerted on the beam by layer stress gradients is given by summing the individual moments exerted by each gradient

$$M_{\text{grad}} = \frac{1}{6} \sum_{i=1}^n w_i t_i^2 \sigma_{i,\text{grad}} (1 - \nu_i), \quad (6)$$

where $\sigma_{i,\text{grad}}$ is the maximum value of the gradient stress. Thus, the radius of curvature, from which the deflection can be calculated, is found from

$$R = \frac{I_{\text{eff}} E_0}{M_{\text{unif}} + M_{\text{grad}}} \quad (7)$$

Equations (1,2,5,6, and 7) constitute a system that allows for the calculation of the radius of curvature of a heated composite beam consisting of any number of layers, each with its own material properties, geometry, and intrinsic stress.

This n-layer model has been compared with FEA simulations of uniformly heated cantilevers having up to seven layers. The parameters used in the simulations are listed in Table I and the results have been plotted in Figure 4. Case 1 and 2 represent a simple thermal actuator layout and only differ by the addition of a 150Å chromium adhesion layer. The effect of this addition is to increase the tip deflection by 12%. This illustrates how significant errors can result from the bimetallic approximation. Case 3 is an arbitrary 5-layer design that the n-layer model estimates with less than 4.5% error from the FEA solution. Case 4 and 5 represent a 7-layer design that clearly cannot be approximated as a bimetallic actuator. The two cases only differ in that the first assumes no intrinsic stresses while second includes the stresses. The intrinsic stresses result in a negative tip deflection at $\Delta T=0$. The analytical solution is within 4% of the FEA solution in both cases.

Array feasibility modeling

The task of modeling thermally actuated DPN probes does not end with the estimation of tip deflection. In real applications, several additional issues must be accommodated to produce

Table I. Geometry and properties of five test beams used in FEA simulations.

Layer	l (Å)	w (μm)	Material	E (GPa)	α (*10 ⁻⁶ /°C)	$\sigma_{i,unif}$ (MPa)
Case 1: 400μm long, $\nu = .3$						
1	3000	50	Si ₃ N ₄	200	2.8	0
2	300	50	Au	80	14.3	0
Case 2: 400μm long, $\nu = .3$						
1	3000	50	Si ₃ N ₄	200	2.8	0
2	150	50	Cr	90	6.0	0
3	300	50	Au	80	14.3	0
Case 3: 1000μm long, $\nu = .33$						
1	5200	100	Si	190	2.6	0
2	2300	90	Au	80	14.3	0
3	6100	130	SiO ₂	67	.35	0
4	4800	120	Ti	110	8.6	.0
5	8900	110	SiO ₂	67	.35	0
Case 4(without stress) and 5(with stress): 1000μm long, $\nu = .3$						
1	6500	45	Au	80	14.3	40
2	500	45	Ti	110	8.6	0
3	5000	50	SiO ₂	67	.35	-20
4	30000	50	Si	190	2.6	0
5	2000	40	SiO ₂	67	.35	-52
6	500	25	Cr	90	6.0	0
7	5000	25	W	344	4.5	-30

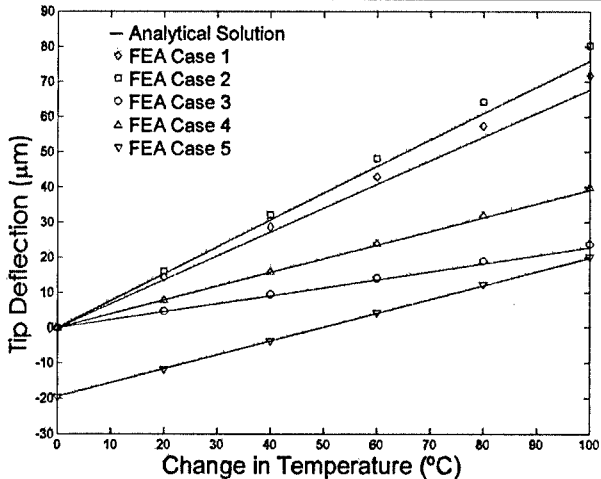


Figure 4. Comparison of probe deflections found using the analytical model, equations (1,2,5,6, and 7), and FEA deflection results. Each case represents a layout as defined in Table I. In all cases, the analytical result differed from the FEA result by less than 6%.

functional devices that will not damage the substrate surface. In most DPN applications, there are at least four ways an array may fail to produce the desired result. The probe may be stiff enough, or the tip sharp enough, to scratch the surface. The intrinsic stresses may be large enough to excessively curl the beam after release. The actuator may not generate enough deflection to overcome tip-to-surface adhesion. Or finally, the actuator may not generate enough deflection to overcome the array overdrive. Overdrive is defined as the additional distance downward, beyond the point of first contact with the substrate, that the array must be pressed to overcome array-to-surface misalignment and irregularities in the tip-to-tip height.

To prevent these failures, the probe geometry and operating parameters can be changed. Unfortunately, many changes will have an opposite impact on the various constraints. For example, increasing the probe stiffness will increase the force it can generate but will also increase the risk of scratching the substrate. The simplicity gained by eliminating the need for individual probe feedback control is offset by the need to carefully evaluate designs before fabrication.

To resolve these conflicting design issues, the n-layer beam model was combined with simple relationships that describe Hertz contact mechanics and capillary adhesion [24] to create an array design simulator [25]. The simulation iterates through a predetermined set of geometries and calculates the probe shape, spring constant, actuator deflection, actuator force, tip adhesion force, and maximum allowable tip down force. This information is used to estimate whether the probe will fail any of above criteria. Designs that pass are plotted against their geometrical parameters to graphically show the relationships between successful layouts.

The results of an example simulation are plotted in Figure 5. The box represents the range of examined actuator designs (approximately 61,000 geometries that differ by length and actuator layer thickness). Designs that pass all the selection criteria (in this case 3,549 or 5.8%) are considered successful and plotted. Failing layouts can also be plotted to show their interrelationships. The plots give a clear visual description of the performance of every design in the design space and allow for a rapid visual evaluation of several optimization schemes.

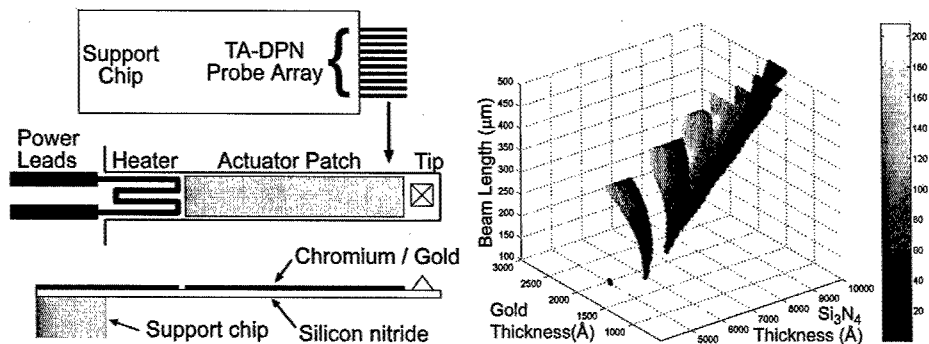


Figure 5. (Left) The simplified layout used in the example feasibility simulation. (Right) A 3-D plot of the successful designs based on the probe layout. Every geometry in the box was simulated and the successful designs were indicated with a shaded dot. The shading indicates the actuator force in percent excess of the minimum necessary to overcome tip-to-surface adhesion. The plot clearly shows the relationship between successful designs and the probe geometry.

Devices

The devices in Figure 3 represent a design that has been optimized across several criteria. The maximum length was fixed at 300 μm to prevent wet release stiction problems. The maximum allowable temperature was limited to 60°C to prevent oxidation of the ODT "ink". Probe stiffness was limited to prevent scratching a gold substrate with a maximum allowable tip-to-substrate angular misalignment of 1 degree. The final design parameters were adjusted to give the greatest chance of a successful design despite minor process variations. To meet these criteria, the devices in Figure 3 have a silicon nitride thickness of 9300 Å and gold thickness of 3650 Å. The probes are 80 μm wide, 295 μm long, and have a tip-to-tip spacing of 100 μm . The analytically estimated spring constant is 0.154 N/m. The heater films have the same thickness as the actuator films.

The thermal performance of the thermally actuated DPN probe is plotted in Figure 6. The typical operating power is approximately 2.5 mW, corresponding to a tip deflection of 10 μm during operation. Analytical modeling indicates that, at this power, the probes reach an average temperature of ~28°C above ambient, which is supported by uniform temperature testing. For chemical inks that are sensitive to heat, the environment can be cooled to allow thermal actuation without excessive temperatures. In our experiments, the binding and friction characteristics of ODT were unaffected by these temperature regimes.

A demonstration of the use of an active probe is shown in Figure 7. In this figure, an active DPN probe was passed through an identical figure-8 pattern several times. The actuator was used to lift the probe from the surface, thus altering the resulting pattern during each run.

A final note concerns tip sharpness. In most AFM applications, tip sharpness is an important issue. During fabrication of our devices, silicon "forms" are coated with silicon nitride to form the tips, thus the tip radius is approximately equal to the nitride film thickness. This can affect the minimum line width and would appear to be a major disadvantage, but we have found that there are several benefits to consider. The overcoat method makes possible a simple and robust fabrication procedure that does not require wafer bonding. The large tip radius also increases the availability of ink near the contact point and greatly reduces the risk of scratching the substrate.

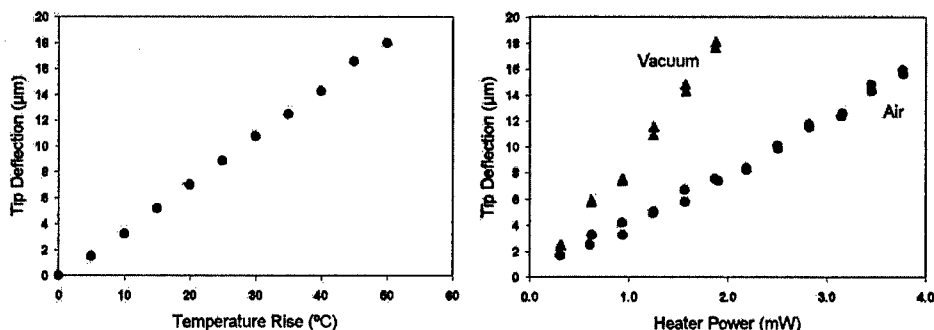


Figure 6. Tip deflection vs. uniform temperature rise and heater power for the devices in Figure 3. Results from two probes are shown in the deflection vs. power plot. The large difference between the vacuum deflection (<300mTorr) and deflection in air illustrates the impact of convection heat transfer on probe performance.

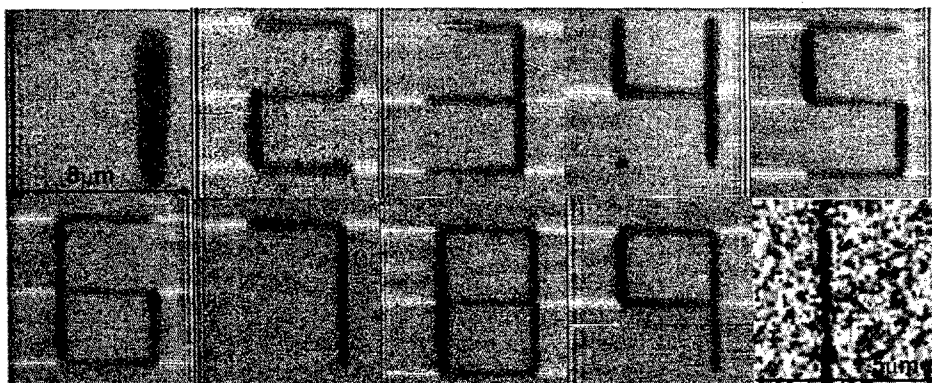


Figure 7. (1-9) $6\text{ }\mu\text{m} \times 4\text{ }\mu\text{m}$ patterns generated by a single thermally actuated DPN probe. Each number was generated by passing the probe through the same figure-8 path and using the thermal actuator to lift the tip as necessary to create the desired pattern. The ODT patterns are written on gold at $.3\text{ }\mu\text{m/sec}$ and imaged using lateral force microscopy with a commercial probe. **(Lower right)** An LFM image of an 80 nm wide ODT line drawn on a gold substrate by an active probe design at $20\text{ }\mu\text{m/sec}$.

This, in turn, allows the system to tolerate greater tip-to-substrate misalignment. The line width issue can be partially remedied by increasing the write speed. In our early testing, as shown in Figure 7, we have achieved a minimum line width of 80 nm at a write speed of $20\text{ }\mu\text{m/sec}$. New designs that combine these advantages with sharper tips are under development.

CONCLUSIONS

We have developed high-density passive and active probe arrays for performing dip pen nanolithography. The probes are produced using a simple and robust fabrication processes, and are capable of producing patterns with sub- 100 nm dimensions. The active probes operate by lifting the probe tip off the surface when their thermal actuators are heated. A performance simulator was created, based on a new n-layer thermal actuator model, to optimize probe designs for the lithography conditions. The resulting designs operate with a power of 2.5 mW per probe, leading to an average temperature rise of approximately 28°C and a tip deflection of $10\text{ }\mu\text{m}$. A demonstration of pattern variation using a thermally actuated probe was also given.

ACKNOWLEDGEMENTS

This work was performed under the Advanced Lithography Program of the Defense Advanced Research Projects Agency (DARPA) (grant DAAD19-00-1-0414). The authors also wish to acknowledge financial support from the Air Force Office of Scientific Research and the Nanoscale Science and Engineering Initiative of the National Science Foundation under NSF Award Number EEC-0118025.

REFERENCES

1. R. Piner, J. Zhu, F. Xu, S. Hong, and C. Mirkin, *Science*, **283**, 661, (1999)
2. L. Demers, D. Ginger, S. Park, Z. Li, S. Chung, C. Mirkin, *Science*, **296**, 1836, (2002)
3. D. Wilson, R. Martin, S. Hong, M. Cronin-Golomb, C. Mirkin, and D. Kaplan, *Proc. Nat. Acad. Sci.*, **98**(24), 13660, (2001).
4. K. Lee, S. Park, C. Mirkin, J. Smith, M. Mrksich, *Science*, **295**, 1702, (2002)
5. M. Su, X. Liu, S. Li, V. P. Dravid, and C. Mirkin, *J. Am. Chem. Soc.*, **124**(8), 1560, (2002).
6. B. Maynor, Y. Li, and J. Liu, *Langmuir*, **17**, 2575, (2001)
7. Y. Li, B. Maynor, and J. Liu, *J. Am. Chem. Soc.*, **123**, 2105, (2001)
8. B. Maynor, S. Filocamo, M. Grinstaff, and J. Liu, *J. Am. Chem. Soc.*, **124**(4), 522, (2002).
9. Ivanisevic and C. Mirkin, *J. Am. Chem. Soc.*, **123**, 7887, (2001)
10. M. Su and V. Dravid, *Appl. Phys. Lett.*, **80**(23), 4434, (2002)
11. D. Weinberger, S. Hong, C. Mirkin, B. Wessels, and T. Higgins, *Adv. Mater.*, **12**(21), 1600, (2000)
12. Hong and C. Mirkin, *Science*, **288**, 1808, (2000)
13. M. Zhang, D. Bullen, and C. Liu, *Proc. of the 2001 1st IEEE Conf. on Nanotechnology*, 27, (2001)
14. M. Zhang, D. Bullen, S. Chung, S. Hong, K. Ryu, Z. Fan, C. Mirkin and C. Liu, *Nanotechnology*, **13**, 212, (2002)
15. C. Liu, R. Gamble, *Sensors Actuators A*, **71**, 233, (1998).
16. S.P. Timoshenko, *J. Opt. Soc. Am.*, **11**, 233, (1925)
17. W-H. Chu, M. Mehregany, R. Mullen, *J. Micromech. Microeng.*, **3**, 4, (1993)
18. Y. Zhang, Y. Zhang, R.B. Marcus, *J. Micromech. Microeng.*, **8**, 43, (1999)
19. V. Pamula, A. Jog, R. Fair, *Tech. Proc. of the MSM 2001 International Conf. on Modeling and Simulation of Microsystems Conf.*, 410, (2001)
20. Y. Min, Y. Kim, *J. Micromech. Microeng.*, **10**, 314, (2000)
21. W. Fang, *J. Micromech. Microeng.*, **9**, 230, (1999)
22. J. Gorrell, P. Holloway, K. Shannon, *Proc. of the Solid State Sensor and Actuator Workshop*, 300, (1998)
23. R.J. Roark, *Roark's Formulas for Stress and Strain*, 6th ed., 117, McGraw-Hill, New York, (1989)
24. B. Bhushan, *Principles and Applications of Tribology*, John Wiley, New York, (1999)
25. D. Bullen, C. Liu, *Proc. SPIE, Smart Electronics, MEMS, and Nanotechnology, SPIE's 9th Annual International Symposium on Smart Structures and Materials*, **4700**, 288, (2002)